

Properties of Defect Modes in One-Dimensional Optically Induced Photonic Lattices

By Francesco Fedele, Jianke Yang, and Zhigang Chen

In this article, localized defect modes in one-dimensional optically induced photonic lattices are studied comprehensively. First, the origin of these defect modes is investigated analytically in the weak-defect limit by perturbation methods. It is shown that in an attractive defect where the lattice light intensity at the defect site is *higher* than that of nearby sites, a defect mode bifurcates from the *left* edge of every Bloch band; while in a repulsive defect, a defect mode bifurcates from the *right* edge of every Bloch band. When the defect is not weak, defect modes are examined by numerical methods. It is shown that in a repulsive defect, the strongest confinement of defect modes arises when the lattice light intensity at the defect site is *nonzero* rather than zero. In addition, as the potential strength increases, defect modes disappear from lower bandgaps and appear in higher bandgaps. In an attractive defect, however, defect modes persist in every bandgap as the potential strength increases. Using a piecewise-constant potential model, defect modes are calculated analytically for a general defect. The analytical results qualitatively explain the main features in numerical results.

1. Introduction

In recent years, light propagation in periodic optical media such as waveguide arrays, optically-induced photonic lattices, and photonic crystals has attracted a

Address for correspondence: Jianke Yang, Zhou-Pei-Yuan Center for Applied Mathematics, Tsinghua University, Beijing 100084, China; e-mail: jyang@cem.uvm.edu

Q1

STUDIES IN APPLIED MATHEMATICS 115:277–299

277

© 2005 by the Massachusetts Institute of Technology

Published by Blackwell Publishing, 350 Main Street, Malden, MA 02148, USA, and 9600 Garsington Road, Oxford, OX4 2DQ, UK.

lot of attention due to their novel physics as well as light-guiding applications [1–15]. Compared to homogeneous media, a new feature in periodic media is the existence of bandgaps inside Bloch bands, where linear light propagation is forbidden. The physical reason for bandgaps is the repeated Bragg reflections of light in the periodic media.

One of the convenient ways to probe the bandgap structure of a periodic medium is to introduce a local defect into the medium. In a repulsive defect where probe light tends to move away from it, if a localized defect mode can be found, then this mode must reside inside the bandgap of the periodic medium. Such a defect mode is trapped by the local defect and can propagate without change of shape. The fact that a repulsive defect can trap a localized defect mode results from a remarkable physical property of wave propagation in periodic structures, which is somewhat against normal intuition. For instance, one would expect light to be guided in a higher index region due to total internal reflections as occurred in a traditional optical fiber. Yet light could be better guided in a lower index region such as an air-hole in a photonic crystal fiber [2]. This unique property can be better understood by the repeated Bragg reflections of optical waves in the periodic medium, just as what happens to electronic waves in semiconductors [1].

Local defects and the corresponding defect modes not only stimulate new physics, but also inspire new applications. For instance, defect modes have been suggested for the guiding and routing of optical signals at very low powers. In addition, linear defect modes in a periodic medium with a local defect are intimately related to nonlinear localized states (solitons) in a uniformly-periodic medium [16]. Indeed, one can view the soliton as a local defect which supports itself as a defect mode [17].

Defect modes have been studied intensively before, mainly in the photonic-crystal community (see [1, 2, 18] for example). In photonic crystals, the refractive-index variation is quite large, which greatly facilitates the creation of defect modes. In “fabricated” one-dimensional waveguides with structured defects, nonlinear defect modes have also been reported and analyzed [19, 20]. Recently, optically induced photonic lattices were successfully generated [9, 21, 22]. In such lattices, the refractive-index variation is several orders of magnitude smaller than that in photonic crystals. In addition, the linear eigenvalue problem for defect modes in photonic lattices is *different* from that in photonic crystals (see [1, 2, 23] and Eq. (4)). Thus one wonders how these differences affect defect modes and their properties in photonic lattices. From a broader perspective, the origin of defect modes is an important issue which has not been well understood so far. How to design local defects to create strongly localized defect modes is another significant issue which has not been investigated in photonic lattices.

In this article, we comprehensively study localized defect modes in one-dimensional optically induced photonic lattices. Using perturbation methods,

we show that defect modes are generically created whenever a weak defect is introduced. If the defect is attractive, i.e., the lattice light intensity at the defect is *higher* than that of nearby sites, a defect mode bifurcates from the *left* edge of every Bloch band. On the other hand, if the defect is repulsive, a defect mode bifurcates from the *right* edge of every Bloch band. When the defect is not weak, we numerically determine defect modes. In repulsive defects, we show that strongly confined defect modes arise when the lattice intensity at the defect site is *nonzero* rather than zero. In addition, as the potential strength increases, defect modes disappear from lower bandgaps and appear in higher bandgaps. In attractive defects, however, defect modes persist in every bandgap as the potential strength increases. Using a piecewise-constant potential model, we determine defect modes analytically for a general defect. The analytical results qualitatively explain the main features of the numerical results.

2. Formulation of the problem

The physical situation we consider is that an ordinarily-polarized or extra-ordinarily-polarized lattice beam with a single-site defect is launched into a photorefractive crystal. This defected lattice beam is assumed to be uniform along the direction of propagation. Meanwhile, an *extra-ordinarily* polarized probe beam with a very low intensity is launched into the defect site, propagating collinearly with the lattice beam. The probe beam is assumed to be mutually incoherent with the lattice beam. In this situation, the nondimensionalized model equation for the probe beam is [8, 24, 25]

$$iU_z + U_{xx} - \frac{E_0}{1 + I_L(x)}U = 0. \quad (1)$$

Here U is the slowly-varying amplitude of the probe beam, z is the propagation distance (in units of $2k_1T^2/\pi^2$), x is the transverse distance (in units of T/π), E_0 is the applied dc field (in units of $\pi^2/(k_0^2n_e^4T^2r_{33})$),

$$I_L = I_0 \cos^2 x \{1 + \epsilon f_D(x)\}, \quad (2)$$

is the intensity function of the photorefractive lattice (normalized by $I_d + I_b$, where I_d is the dark irradiance of the crystal and I_b the background illumination), I_0 is the peak intensity of the otherwise uniform photonic lattice (i.e., far away from the defect site), $f_D(x)$ is a localized function describing the shape of the defect, ϵ controls the strength of the defect, T is the lattice spacing, $k_0 = 2\pi/\lambda_0$ is the wavenumber (λ_0 is the wavelength), $k_1 = k_0n_e$, n_e is the unperturbed refractive index, and r_{33} is the electro-optic coefficient of the crystal. The dark irradiance I_d corresponds to the thermal generation of electrons in a photorefractive crystal kept in dark (no light illumination). In typical experiments on photorefractive crystals, the background illumination

$I_b \gg I_d$, thus $I_d + I_b \approx I_b$. In this paper, we assume that the defect is restricted to a single lattice site at $x = 0$. Thus, we choose function $f_D(x)$ as

$$f_D(x) = \exp(-x^8/128).$$

Other choices of single-site defect functions f_D give similar results. When $\epsilon < 0$, the lattice light intensity I_L at the defect site is lower than that at the surrounding sites. We call it a repulsive (negative) defect where light tends to escape from the defect to nearby lattice sites. For $\epsilon = -0.08, -0.5, -0.81$, and -1 , the corresponding lattice intensity profiles are displayed later in the text (see Figures 5 and 8). When $\epsilon = -1$, the lattice has no light at the defect site, while in the other three cases, it still has light at the defect site but with a reduced intensity. When $\epsilon > 0$, the defect is called an attractive (positive) defect where the lattice intensity I_L at the defect site is higher than that at the surrounding sites. The defect profile at $\epsilon = 1$ is displayed in Figure 11. Experimental creation of these lattices with attractive or repulsive defects by use of the optical induction method is currently underway. Consistent with our previous experiments [12], we choose parameters as follows: the lattice intensity $I_0 = 3I_b$, lattice spacing $T = 20 \mu\text{m}$, $\lambda_0 = 0.5 \mu\text{m}$, $n_e = 2.3$, and $r_{33} = 280 \text{ pm/V}$. Then one x unit corresponds to $6.4 \mu\text{m}$, one z unit corresponds to 2.3 mm , and one E_0 unit corresponds to 20 V/mm in physical units.

Defect modes in Equation 1 are sought in the form

$$U(x, z) = e^{-i\mu z} u(x), \quad (3)$$

where function $u(x)$ is localized in x and satisfies the linear equation

$$u''(x) + \left(\mu - \frac{E_0}{1 + I_L(x)} \right) u = 0 \quad (4)$$

and μ is a propagation constant. Numerically, these modes can be determined by expanding the solution $u(x)$ into discrete Fourier series and then converting Equation (4) into a matrix eigenvalue problem with μ as the eigenvalue.

To analyze defect modes in Equation (4), it is necessary to first understand the dispersion relation and bandgap structure of a uniform lattice (i.e., $\epsilon = 0$ in Equation (2)). In a uniform lattice, the Floquet theory says that the solution of Equation (4) is of the form

$$u(x) = e^{ikx} p(x; \mu), \quad (5)$$

where $p(x; \mu)$ is a periodic function in x with the same period π as the potential term I_L , and $\mu = \mu(k)$ is the dispersion relation. It is well known that the dispersion relation contains an infinite number of branches in the first Brillouin zone $-1 \leq k \leq 1$. Each branch corresponds to a Bloch band. The gaps between adjacent branches are the bandgaps. At $E_0 = 6$ and $I_0 = 3$, this dispersion relation is displayed in Figure 1, while the bandgap structure

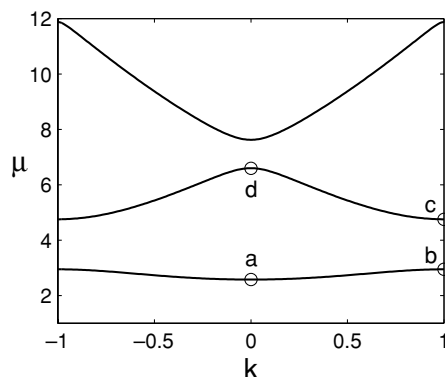


Figure 1. Dispersion relation of a uniform lattice at $E_0 = 6$ and $I_0 = 3$. Bloch states at circled locations are displayed in Figure 3.

at various values of E_0 is presented in Figure 2. The semi-infinite bandgap, which is to the far left, is the bandgap which persists when the photonic lattice is removed. We will call the bandgap next to the semi-infinite bandgap as the first bandgap, and the next one as the second bandgap, and so on.

Bloch states on the edges of Bloch bands are also important because, as we will see below, defect modes will bifurcate from such Bloch states under weak-defect perturbations. On these edges, $k = 0$ or $k = \pm 1$. If $k = 0$, the Bloch solution (5) is periodic with period π ; if $k = \pm 1$, it is also periodic but with period 2π . In Figure 3, the first four Bloch states at $E_0 = 6$ are displayed. Of these four states, the first two are symmetric, and the last two antisymmetric, in x .

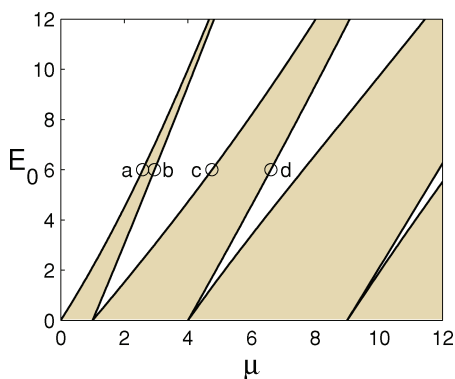


Figure 2. Bandgap structure of a uniform lattice at $I_0 = 3$. The shaded region is the Bloch bands. Bloch solutions at circled locations are displayed in Figure 3.

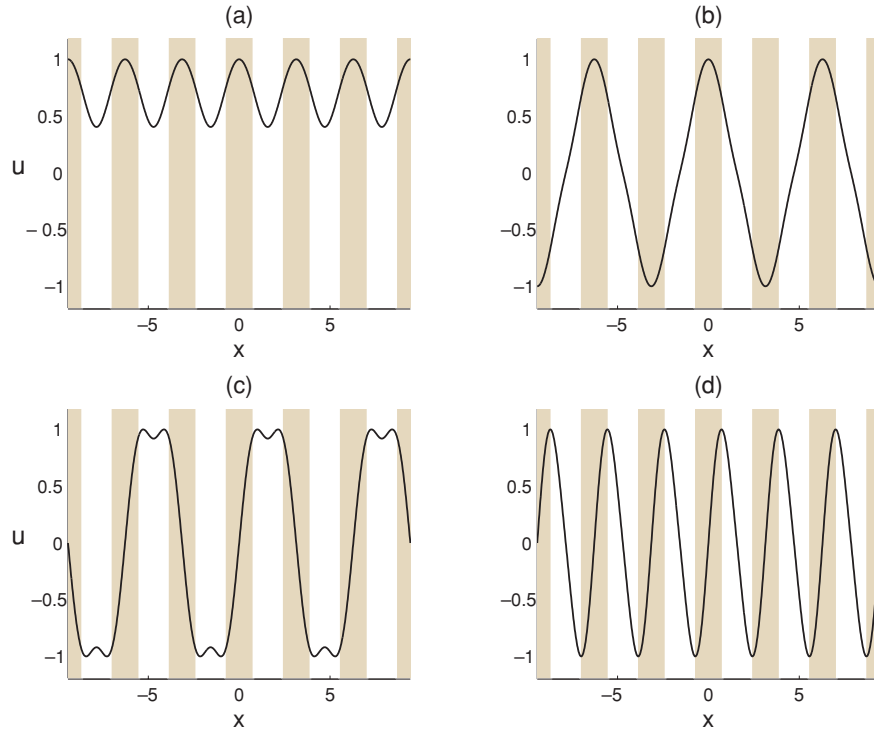


Figure 3. The first four Bloch states $u(x)$ at the edges of Bloch bands in a uniform lattice with $E_0 = 6$ and $I_0 = 3$. These Bloch states correspond to points marked as circles in Figures 1 and 2. The μ values are $\mu = 2.5781$ in (a), 2.9493 in (b), 4.7553 in (c), and 6.6011 in (d), respectively. The shaded stripes in these plots represent the locations of waveguides corresponding to high intensities in the lattice.

3. Bifurcation of defect modes under weak defects

One of the main theoretical questions on defect modes is their origin, i.e., where do defect modes bifurcate from? In this section, we analytically investigate this question in the limit of weak defects where $\epsilon \ll 1$ in Equation (2). We will show that when $0 \neq \epsilon \ll 1$, an infinite number of defect modes, one in each bandgap, bifurcate out from the edges of Bloch bands. If $\epsilon > 0$ (attractive defect), defect modes bifurcate simultaneously from the left edge of each Bloch band, while if $\epsilon < 0$ (repulsive defect), defect modes bifurcate simultaneously from the right edge of each Bloch band. We will also derive the eigenvalues of these defect modes asymptotically, and show that these analytical formulas are in good agreement with the numerical data. The analytical technique we will use is a perturbation method which is stimulated by the treatment of internal modes in nonlinear wave systems [27].

Consider the general one-dimensional perturbed Hill's equation

$$\frac{d^2\psi}{dx^2} + [\mu + V(x)]\psi = \epsilon f(x)\psi, \quad (6)$$

where $V(x)$ is a T -periodic function, $f(x)$ is a localized defect function, and $\epsilon \ll 1$. When $\epsilon = 0$, Equation (6) admits Floquet solutions of the form $e^{ikx}g(x; \mu_n(k))$, where $\mu = \mu_n(k)$ is the dispersion relation of the n -th Bloch band, k is in the first Brillouin zone $[-\pi/T, \pi/T]$, and $g(x; \mu_n(k))$ is a T -periodic function in x . All these Floquet modes $\{e^{ikx}g(x; \mu_n(k)), k \in [-\pi/T, \pi/T], n = 1, 2, \dots\}$ form a complete set [26]. In addition, the orthogonality condition between these Bloch modes is

$$\int_{-\infty}^{\infty} e^{-i(k_1-k_2)x} g^*(x; \mu_n(k_1))g(x; \mu_m(k_2)) dx = 2\pi \delta(k_1 - k_2)\delta(n - m). \quad (7)$$

Here the Bloch functions have been normalized by

$$\frac{\int_0^T |g(x; \mu_n(k))|^2 dx}{T} = 1,$$

$\delta(\cdot)$ is the δ -function, and the superscript “*” represents complex conjugation. When $\epsilon \neq 0$, localized eigenfunctions at discrete eigenvalues μ inside the gaps of Bloch bands arise in Equation (6). These localized eigenmodes are called defect modes, and their asymptotic expressions will be derived below.

When $\epsilon \neq 0$, the defect modes can be expanded into Bloch waves as

$$\psi(x) = \sum_{n=1}^{\infty} \int_{-\pi/T}^{\pi/T} \alpha_n(k) e^{ikx} g(x; \mu_n(k)) dk, \quad (8)$$

where $\alpha_n(k)$ is an unknown function to be determined. The integral equation for $\alpha_n(k)$ can be obtained by substituting Equation (8) into (6), which yields

$$\alpha_n(k)(\mu - \mu_n(k)) = \frac{1}{2\pi} \epsilon \sum_{m=1}^{\infty} \int_{-\pi/T}^{\pi/T} \alpha_m(\kappa) W_{m,n}(k, \kappa) d\kappa, \quad (9)$$

where the kernel $W_{m,n}(k, \kappa)$ is given by

$$W_{m,n}(k, \kappa) = \int_{-\infty}^{\infty} e^{-i(k-\kappa)x} g^*(x; \mu_n(k)) f(x) g(x; \mu_m(\kappa)) dx.$$

Denote

$$\phi_n(k) = \alpha_n(k)(\mu - \mu_n(k)),$$

then this integral equation transforms to

$$\phi_n(k) = \frac{1}{2\pi} \epsilon \sum_{m=1}^{\infty} \int_{-\pi/T}^{\pi/T} \phi_m(\kappa) \frac{W_{m,n}(k, \kappa)}{\mu - \mu_m(\kappa)} d\kappa. \quad (10)$$

Suppose the defect mode bifurcates from an edge point $\mu = \mu_c$ of the n -th Bloch band, and the defect eigenvalue has the asymptotic expansion

$$\mu = \mu_c + \beta\epsilon^2 + O(\epsilon^3), \quad (11)$$

where β is a constant to be determined. It is noted that at the edge point $\mu = \mu_c$, $k = 0$ or $\pm\pi$, and $\mu'_n(k) = 0$. First, we consider the $k = 0$ case (the other case will be treated in the end). The dispersion relation near this edge point can be expanded as

$$\mu_n(k) = \mu_c + \frac{1}{2}\mu''_n(0)k^2 + O(k^4). \quad (12)$$

When Equations (11) and (12) are substituted into Equation (10), we see that only one integral in the summation with index $m = n$ makes $O(1)$ contribution, and the rest of the integrals give $O(\epsilon)$ contribution. Thus,

$$\phi_n(k) = \frac{1}{2\pi}\epsilon \int_{-\pi/T}^{\pi/T} \phi_n(\kappa) \frac{W_{n,n}(k, \kappa)}{\mu - \mu_n(\kappa)} d\kappa + O(\epsilon). \quad (13)$$

Note that the first term in the above equation is $O(1)$ rather than $O(\epsilon)$, as we will see below. For the denominator in the integral of Equation (13) not to vanish on the k interval $[-\pi/T, \pi/T]$, we must require that $\text{sgn}(\beta) = -\text{sgn}[\mu''_n(0)]$. In that case, the denominator will have zeros at

$$k = \pm ik_0|\epsilon| + O(\epsilon^2), \quad k_0 \equiv \sqrt{\frac{2|\beta|}{|\mu''_n(0)|}}. \quad (14)$$

Hence, the integral in Equation (13) can be evaluated by residues after its contour is closed by an upper semicircle of radius 1. The integral on this semicircle gives $O(\epsilon)$ contribution, while the residue gives $O(1)$ contribution. After simple calculations, Equation (13) becomes

$$\phi_n(k) = -\frac{\text{sgn}(\epsilon)}{k_0\mu''_n(0)}\phi_n(ik_0|\epsilon|)W_{n,n}(k, ik_0|\epsilon|) + O(\epsilon). \quad (15)$$

Now we take $k = ik_0|\epsilon|$ in the above equation. This equation is consistent only if

$$\text{sgn}(\epsilon) = -\text{sgn}[W_{n,n}(0, 0)\mu''_n(0)]. \quad (16)$$

In that case, we get the coefficient β in the defect-eigenvalue formula (11) as

$$\beta = -\frac{|W_{n,n}(0, 0)|^2}{2\mu''_n(0)}, \quad (17)$$

where

$$W_{n,n}(0, 0) = \int_{-\infty}^{\infty} f(x)|g(x; \mu_n(0))|^2 dx. \quad (18)$$

Equations (11), (16), and (17) give the bifurcation conditions for defect modes as well as their leading-order expressions.

In the above calculations, defect modes are assumed to bifurcate from the edge point of a Bloch band where $k = 0$. If the defect mode bifurcates rather from the edge of a Bloch band where $k = \pm \pi/T$, then the only modification to the above results is that the μ_n and μ_n'' terms in Equations (17) and (18) are evaluated at $k = \pi/T$ rather than $k = 0$. More specifically, the bifurcation condition in this case is

$$\text{sgn}(\epsilon) = -\text{sgn}[W_{n,n}(\pi/T, \pi/T)\mu_n''(\pi/T)], \quad (19)$$

and the constant β in the defect-mode formula (11) is given by

$$\beta = -\frac{|W_{n,n}(\pi/T, \pi/T)|^2}{2\mu_n''(\pi/T)}, \quad (20)$$

where

$$W_{n,n}(\pi/T, \pi/T) = \int_{-\infty}^{\infty} f(x)|g(x; \mu_n(\pi/T))|^2 dx. \quad (21)$$

Finally, we apply the above analysis to Equation (4). When $\epsilon \ll 1$, Equation (4) can be expanded as

$$u''(x) + \left(\mu - \frac{E_0}{1 + I_0 \cos^2 x} \right) u = \epsilon f(x)u + O(\epsilon^2), \quad (22)$$

where

$$f(x) = -\frac{E_0 I_0 \cos^2 x f_D}{(1 + I_0 \cos^2 x)^2}. \quad (23)$$

If $E_0 > 0$, this function is always negative, thus $W_{n,n}(k, k) < 0$. Then Equations (16) and (19) indicate that bifurcation of defect modes from an edge point of a Bloch band is possible only if ϵ has the same sign as μ'' (or the curvature) of the dispersion curve at the edge point. For the present model (4), all the curvatures at the left (lower) edge points of Bloch bands have the positive sign, while those at the right (upper) edge points have the negative sign (see Figure 1). Thus defect-mode bifurcation is possible at all lower edge points of Bloch bands when $\epsilon > 0$ (i.e., attractive defect), while it is possible at all upper edge points of Bloch bands when $\epsilon < 0$ (i.e., repulsive defect). The leading-order asymptotic formulae (11), (17), and (20) for the first four branches of defect modes are plotted in Figure 4 (as dashed lines).

To verify these analytical results for weak defects, and more importantly, to investigate defect modes when the defect is not weak, we now study defect modes numerically. To be specific, we fix $E_0 = 6$, and let ϵ vary from -1 to 1 . We have obtained the defect modes at each ϵ value, and the entire diagram of defect eigenvalues versus ϵ is plotted in Figure 4 (as solid lines).

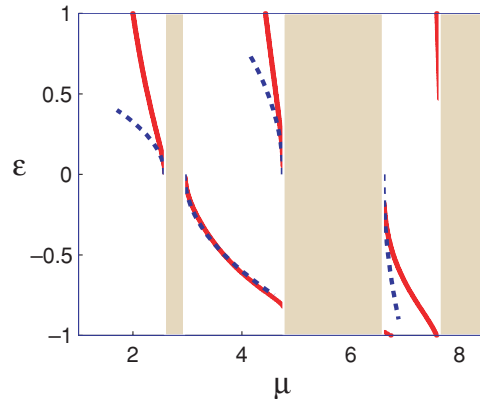


Figure 4. Bifurcation of defect modes with defects (2) at $E_0 = 6$ and $I_0 = 3$. Solid lines: numerical results; dashed lines: analytical results. The shaded region is the Bloch bands.

We see that when ϵ increases from zero, a defect mode bifurcates from the left edge of each Bloch band into the bandgap. On the other hand, when ϵ decreases from zero, a defect mode bifurcates from the right edge of each Bloch band into the bandgap. In the latter case, there are no defect modes in the semi-infinite bandgap. These results agree perfectly with the above perturbation analysis. Good quantitative agreement between the asymptotic formula (11) and numerical values can be observed in Figure 4 as well, especially at small ϵ values. When $|\epsilon|$ is not small, an interesting phenomenon in Figure 4 is that a defect branch can merge into the edge of a Bloch band and disappears. This happens with repulsive defects ($\epsilon < 0$). For instance, the branch in the first bandgap terminates on the right edge of the bandgap at $\epsilon \approx -0.83$. This implies that strong repulsive defects not necessarily favor the creation of defect modes.

We would like to make a remark here. The above results on defect-mode bifurcations are closely related to the bifurcation of gap solitons in a uniform periodic lattice [16]. In that situation, it was shown that for focusing nonlinearity, small-amplitude gap solitons bifurcate from the left edge of each Bloch band, while for defocusing nonlinearity, small-amplitude gap solitons bifurcate from the right edge of each Bloch band. If one considers a gap soliton as a defect in a uniform lattice, then our results and those in [16] agree in spirit. Minor differences exist between the two cases though. For instance, in the gap-soliton case, *two* gap solitons bifurcate out together from the edge of a Bloch band, while in the present case, only one defect mode bifurcates out. The reason is that in the gap-soliton case, due to the uniformity of the lattice (no defects), the center of gap solitons can be either on-site or off-site. But in the present case, the defect destroys the uniformity of the lattice, and the center of defect modes is always at the center of the defect.

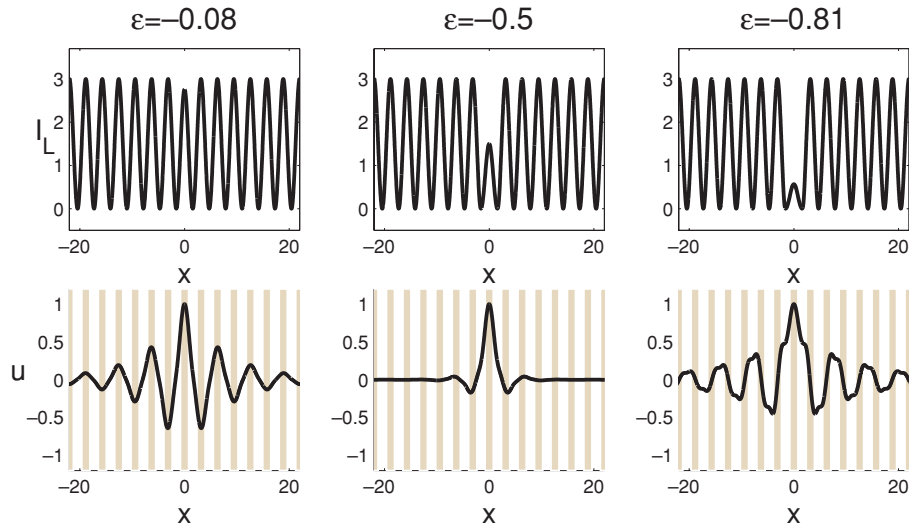


Figure 5. Upper row: intensities of three defected photonic lattices with $\epsilon = -0.08$, -0.5 , and -0.81 ; lower row: the corresponding defect modes $u(x)$ in the first bandgap. The shaded stripes in the lower row represent the locations of large lattice intensities. Here $E_0 = 6$ and $I_0 = 3$.

4. Strongly confined defect modes in repulsive defects

For some applications, it is often desirable to create defect modes that are strongly confined at the defect. If the defect is attractive, defect modes are generally more confined if the defect is stronger (i.e., ϵ is larger in Equation (2)). This is because an attractive defect acts like a waveguide—the stronger it is, the deeper the waveguide is, and hence the more confined the defect mode is. But with repulsive defects, do stronger defects give more confined defect modes? Apparently not. To demonstrate, let us consider the defect-mode branch in the first bandgap of Figure 4. This branch exists when $-0.83 < \epsilon < 0$. At three representative ϵ values -0.08 , -0.5 and -0.81 , the lattice-intensity profiles and the corresponding defect modes are displayed in Figure 5. We see that when $|\epsilon|$ is small, the defect mode is rather weakly confined because the defect eigenvalue is rather close to the right edge of the first Bloch band (see Fig. 5, left column). As $|\epsilon|$ increases, the mode becomes more confined (see Fig. 5, middle column). As ϵ approaches -0.83 , however, the defect eigenvalue approaches the left edge of the second Bloch band, and the defect mode becomes less confined again (see Fig. 5, right column). The strongest confinement of defect modes is found when $\epsilon \approx -0.5$ (see Fig. 5, middle column). These findings are rather interesting, as they show that the most localized defect mode arises when the lattice intensity at the defect site is *nonzero* rather than zero. Such results may have important implications for applications of defect modes in photonic lattices.

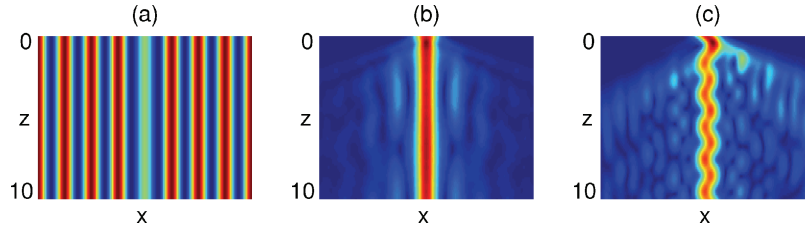


Figure 6. Evolution of (a) Gaussian beam launched at zero (b) and non-zero (c) angles into a defected photonic lattice (a). Here $I_0 = 3$, $E_0 = 6$, and $\epsilon = -0.5$ in Equation (1). The initial phase gradient in (c) is $k = 1$.

The existence of localized defect modes in photonic lattices with repulsive defects is an interesting phenomenon which merits experimental verification. In experiments, if the input probe beam takes the profile of a defect mode and is launched at zero angle into the defect site, then it will propagate stationarily and not diffract at all. However, Gaussian input beams are more customary in experiments. In addition, the launch angle may not be precisely zero. Thus it is desirable to investigate the evolution of a Gaussian input beam launched at small angles into a defect and determine if the beam can be trapped by a repulsive defect or not. For this purpose, we simulate Equation (1) numerically with $I_0 = 3$, $E_0 = 6$, and $\epsilon = -0.5$, and take the initial condition as a tilted Gaussian beam

$$U(x, 0) = e^{-\frac{1}{2}x^2 + ikx}, \quad (24)$$

whose intensity profile resembles the central hump of the defect mode at $E_0 = 6$ and $\epsilon = -0.5$ (see Fig. 5, lower middle panel). The phase gradient k here is proportional to the launch angle of the Gaussian beam. Our simulation uses the pseudo-spectral method. At zero launch angle ($k = 0$), we found that a vast majority of the input-beam's energy is trapped inside the defect and propagates stationarily (see Fig. 6(b)). Next we take $k = 1$, which corresponds to a launch angle of 0.58° with physical parameters listed earlier. In this case, most of the probe light is still trapped inside the defect site. However, the trapped probe light undergoes robust snake-like oscillations as it propagates through the defect (see Fig. 6(c)). Regarding the origin of these oscillations, we found that they are due to the beating between two defect modes existing in the first and second bandgaps at $\epsilon = -0.5$ (see Fig. 4). Indeed, these defect modes have $\mu^a = 3.664$ and $\mu^b = 6.782$, whose beating period $2\pi/(\mu^b - \mu^a) = 2.01$ is very close to the observed period of oscillations in (c).

5. Dependence of defect modes on the applied dc field E_0

In this section, we examine how the applied dc field value E_0 affects defect modes. We will consider the repulsive and attractive defects separately. For

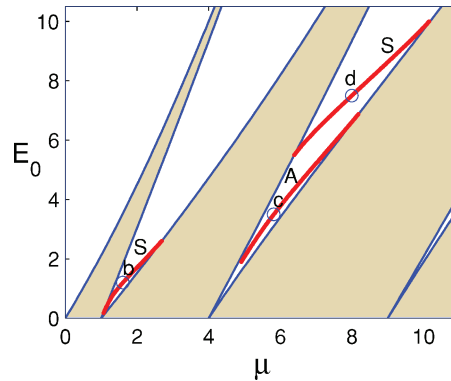


Figure 7. Defect eigenvalues versus the applied dc field parameter E_0 for a repulsive defect with $\epsilon = -1$ and $I_0 = 3$. The shaded region is the Bloch bands. Letters “S” and “A” indicate branches of symmetric and antisymmetric defect modes. Defect modes at points marked by circles and labeled by letters “b, c, d” are displayed in Figures 8(b)–(d), respectively.

simplicity, we fix $\epsilon = \pm 1$, and examine defect modes at various values of E_0 . At other ϵ values, the defect-mode behavior is expected to be qualitatively the same.

5.1. Repulsive-defect case

First, we consider the repulsive defect with $\epsilon = -1$, where the lattice intensity at the defect is zero (see Fig. 8(a)). For this defect, we have obtained the defect modes at various values of E_0 , and the results are displayed in Figures 7 and 8. In Figure 7, eigenvalues μ of the defect modes are shown. It is seen that these defect eigenvalues lie inside bandgaps of the uniform photonic lattice. In addition, each branch of the defect modes is born on one boundary of a bandgap, and dies on the other boundary as E_0 varies. Specifically, the branch in the first bandgap exists when $0 < E_0 < 2.8$; the lower branch in the second bandgap exists when $0 < E_0 < 7.5$; while the upper branch in the second bandgap exists when $5.3 < E_0 < 10.3$. Note that these defect states do not exist in the semi-infinite bandgap. More interestingly, when the applied voltage E_0 increases, defect modes disappear from lower bandgaps and appear in higher bandgaps. In other words, defect modes move from lower bandgaps to higher ones as E_0 increases. In Figure 8, three defect modes on three different branches are displayed. Their corresponding (E_0, μ) values are marked as circles in Figure 7. Of these three defect modes, the one in Figure 8(d) is relatively confined, while the other two are quite broad. Figure 8 also reveals that the lower branch in the second bandgap of Figure 7 gives antisymmetric defect modes, while the other two branches give symmetric defect modes.

The existence of these defect modes as well as their shape and symmetry properties have a profound effect on linear probe-light propagation in the

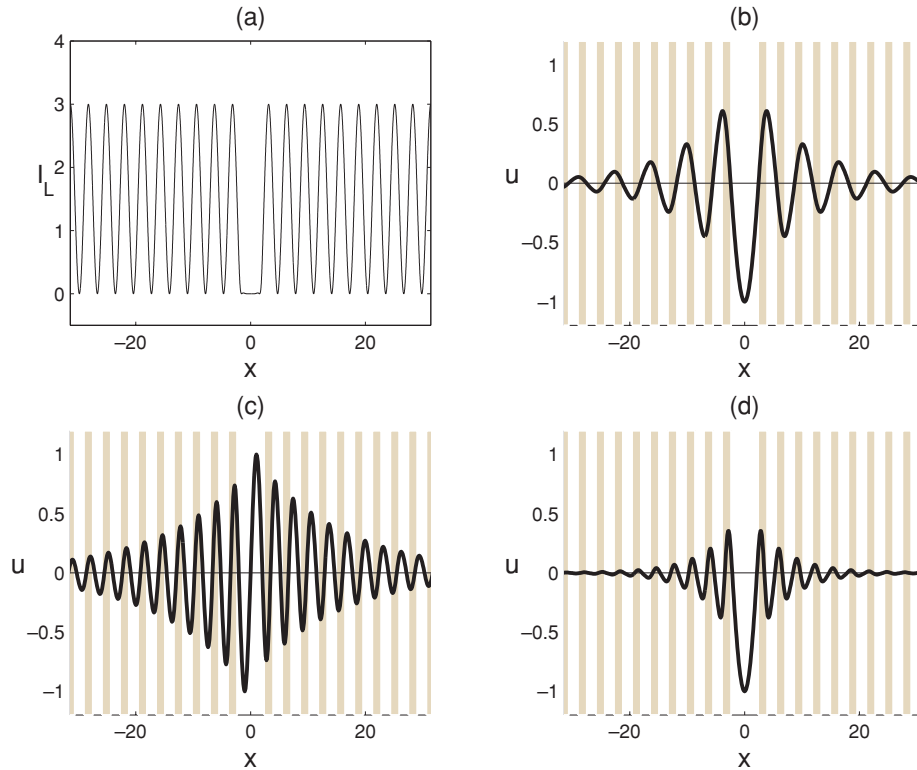


Figure 8. (a) Intensity profile $I_L(x)$ of a photonic lattice with a repulsive defect of $\epsilon = -1$. (b–d) three defect modes at (μ, E_0) values marked by circles in Figure 7. Specifically, $(E_0, \mu) = (1.2, 1.6042)$ in (b), $(3.5, 5.8122)$ in (c), and $(7.5, 7.9974)$ in (d). The shaded stripes in (b–d) represent the locations of large lattice intensities. Here $I_0 = 3$.

underlying defected photonic lattices. For a Gaussian input beam, its evolution critically depends on whether a defect mode resembling the input Gaussian beam exists under the same physical conditions. To demonstrate, we take an initial Gaussian beam as

$$U(x, 0) = e^{-\frac{1}{3}x^2},$$

which resembles the central hump of the defect mode in Figure 8(d), and simulate its evolution under various E_0 values. The simulation results at five representative E_0 values 0, 1.5, 5, 7.5, and 10 are displayed in Figure 9(b)–(f), while the lattice intensity field is shown in Figure 9(a) (which is the same as that in Fig. 8a but plotted differently). At small values of E_0 , we found that the Gaussian beam strongly diffracts and quickly becomes invisible (see Fig. 9(b, c)). Similar behavior persists as E_0 increases (see Fig. 9d) until it reaches a value of about 7.5, when a large portion of the initial beam’s energy is trapped inside the defect site and propagates stationarily (see Fig. 9(e)). As

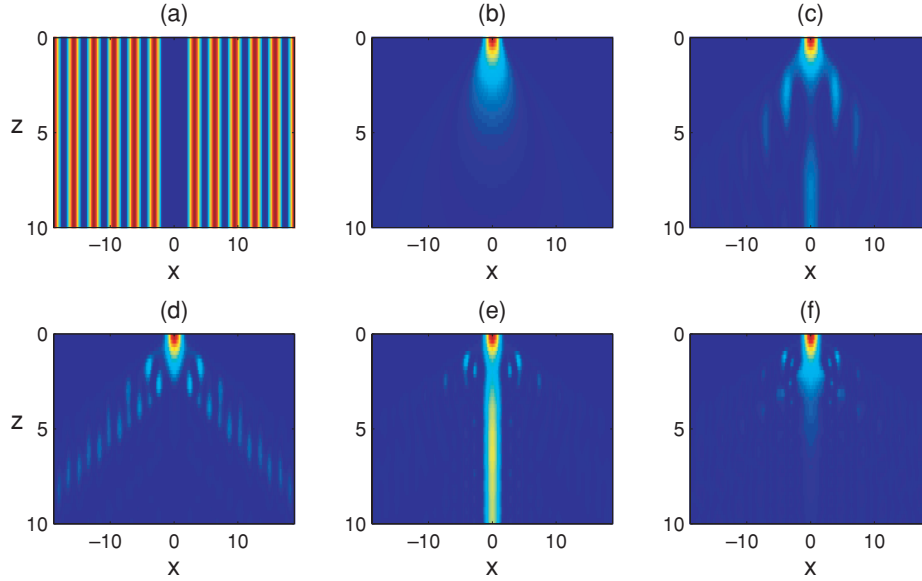


Figure 9. Evolution of a Gaussian beam in a photonic lattice with a repulsive defect of $\epsilon = -1$ at $I_0 = 3$ and various values of E_0 . (a) intensity field of the lattice; (b–f) evolutions of a Gaussian beam at $E_0 = 0, 1.5, 5, 7.5,$ and 10 , respectively.

E_0 increases beyond 7.5 , however, strong diffraction of the probe beam is seen again (see Fig. 9(f)). Hence, an optimal lattice potential as controlled here by E_0 could better trap defect modes. These results indicate that the trapping of the probe light in Figure 9(e) could not be attributed to either the simple guidance due to increased lattice potential or the nonlinear self-action of the probe beam itself. Rather it must be attributed to the repeated Bragg reflections inside the photonic lattice under certain phase-matching conditions, as the Gaussian beam matches the localized mode of the defect. This bears strong resemblance to localized modes in photonic crystals [1, 2, 23].

5.2. Attractive-defect case

Next, we consider the case of attractive defects. We fix $\epsilon = 1$ and $I_0 = 3$, and consider the effect of the dc field E_0 on defect modes. The lattice-field profile for this ϵ value can be seen in Figure 11(a). In this case, the usual light-guiding theory predicts one defect mode that is largely confined in the defect. This is confirmed in Figure 10, where the branch of defect modes in the semi-infinite bandgap is the one we normally anticipate. What is interesting is that in addition to this expected defect mode, a number of other defect modes appear in higher bandgaps as well. All these branches of defect modes persist when E_0 increases, in contrast with the repulsive ($\epsilon < 0$) case where defect-mode branches terminate as E_0 increases. In Figure 11, three defect

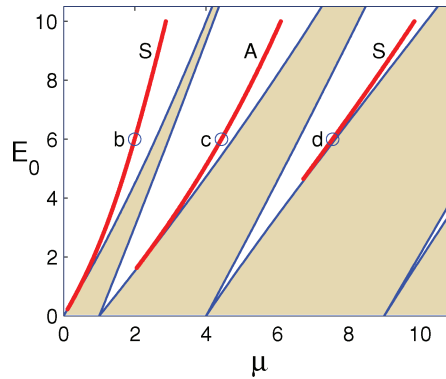


Figure 10. Defect eigenvalues μ versus the applied dc field parameter E_0 for an attractive defect with $\epsilon = 1$ and $I_0 = 3$. The shaded region is the Bloch bands. Letters “S” and “A” indicate branches of symmetric and antisymmetric defect modes. Defect modes at points marked by circles and labeled by letters “b, c, d” are displayed in Figures 11(b)–(d) respectively.

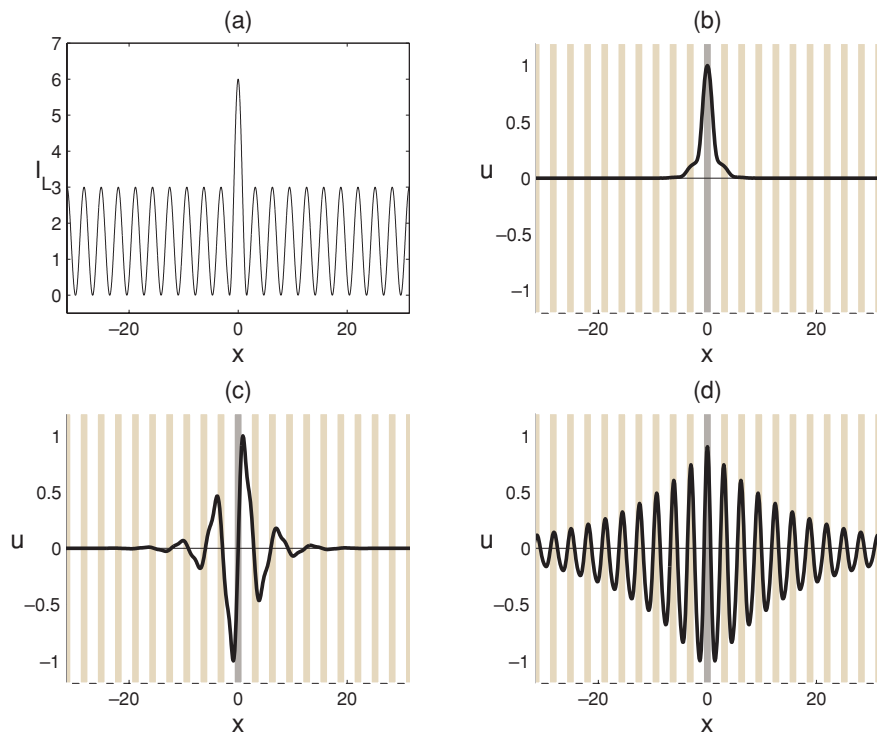


Figure 11. (a) Intensity profile of a photonic lattice with an attractive defect of $\epsilon = 1$. (b–d) three defect modes at (μ, E_0) values marked by circles in Figure 10. Specifically, $(E_0, \mu) = (6, 1.9912)$ in (b), $(6, 4.4278)$ in (c), and $(6, 7.5518)$ in (d). The shaded stripes in (b–d) represent the locations of large lattice intensities. Here $I_0 = 3$.

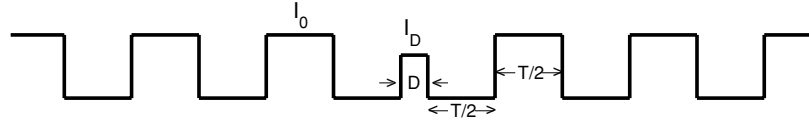


Figure 12. Schematic profile of a piecewise-constant periodic potential $I_L(x)$ with a defect.

modes at $E_0 = 6$ are displayed. The first one in the semi-infinite bandgap is quite localized. Those in higher bandgaps are broader, mainly because their eigenvalues are closer to the edges of bandgaps.

6. Defect modes in piecewise-constant potentials

In the above section, we observed some interesting features in defect modes. For instance, with a repulsive defect, each branch of defect modes appears or disappears as E_0 increases. To better understand these behaviors, in this section, we use a piecewise-constant potential to approximate the one in (2). By doing so, we could calculate defect modes analytically, which will provide much insight on properties of defect modes. In photonic crystals, defect modes in piecewise-constant potentials have been analytically obtained [1, 2, 23]. But the eigenvalue problem there is different from the one in Equation (4) here, thus their results could not be copied over.

The piecewise-constant potential we use is illustrated in Figure 12, where

$$I_L(x) = \begin{cases} 0, & nT + \frac{1}{2}D < |x| < (n + \frac{1}{2})T + \frac{1}{2}D, & n = 0, 1, 2, \dots, \\ I_0, & (n + \frac{1}{2})T + \frac{1}{2}D < |x| < (n + 1)T + \frac{1}{2}D, & n = 0, 1, 2, \dots, \\ I_D, & |x| < \frac{1}{2}D, \end{cases} \quad (25)$$

T and I_0 are the period and light intensity of the lattice away from the defect, and D and I_D are the length and intensity of the defect site. For convenience, we cast Equation (4) in the form

$$u_{xx} + \{\mu + V(x)\}u = 0. \quad (26)$$

Then, the potential function $V(x) = -E_0/\{1 + I_L(x)\}$ is the following piecewise-constant function

$$V(x) = \begin{cases} V_1, & nT + \frac{1}{2}D < |x| < (n + \frac{1}{2})T + \frac{1}{2}D, & n = 0, 1, 2, \dots, \\ V_2, & (n + \frac{1}{2})T + \frac{1}{2}D < |x| < (n + 1)T + \frac{1}{2}D, & n = 0, 1, 2, \dots, \\ V_D, & |x| < \frac{1}{2}D, \end{cases} \quad (27)$$

where

$$V_1 = -E_0, \quad V_2 = -\frac{E_0}{1 + I_0}, \quad V_D = -\frac{E_0}{1 + I_D}. \quad (28)$$

To calculate defect modes in this potential, we first construct the transfer matrix M of the uniformly-periodic lattice (without the defect) from the beginning to the end of an interval of length T . Because this matrix depends on the starting point of the T -length interval, we set this interval to start at the beginning of a V_1 cell. Simple calculations show that the corresponding transfer matrix M is

$$M = \begin{pmatrix} M_{11} & M_{12} \\ M_{21} & M_{22} \end{pmatrix}, \quad (29)$$

where

$$M_{11} = \cos \theta_1 \cos \theta_2 - \frac{\sqrt{\mu + V_1}}{\sqrt{\mu + V_2}} \sin \theta_1 \sin \theta_2, \quad (30)$$

$$M_{12} = \frac{1}{\sqrt{\mu + V_1}} \sin \theta_1 \cos \theta_2 + \frac{1}{\sqrt{\mu + V_2}} \cos \theta_1 \sin \theta_2, \quad (31)$$

$$M_{21} = -\sqrt{\mu + V_1} \sin \theta_1 \cos \theta_2 - \sqrt{\mu + V_2} \cos \theta_1 \sin \theta_2, \quad (32)$$

$$M_{22} = \cos \theta_1 \cos \theta_2 - \frac{\sqrt{\mu + V_2}}{\sqrt{\mu + V_1}} \sin \theta_1 \sin \theta_2, \quad (33)$$

and

$$\theta_1 = \frac{1}{2}T\sqrt{\mu + V_1}, \quad \theta_2 = \frac{1}{2}T\sqrt{\mu + V_2}. \quad (34)$$

It can be easily checked that $\det(M) = 1$. Thus, the eigenvalues of matrix M are

$$\lambda = \frac{1}{2} \left[\text{Tr}(M) \pm \sqrt{\text{Tr}^2(M) - 4} \right], \quad (35)$$

while the Floquet exponent ik of a uniform lattice (as in Equation (5)) is given by the relation

$$e^{ikT} = \lambda. \quad (36)$$

For μ to be inside a Bloch band, solution k of the above equation must be purely real. Thus, Bloch bands are specified by the relation $|\text{Tr}(M)| \leq 2$, and $\text{Tr}(M) = \pm 2$ gives band edges. The dispersion relation $\mu = \mu(k)$ of a uniform lattice follows from Equation (36) as $\cos kT = \frac{1}{2}\text{Tr}(M)$, i.e.,

$$\cos kT = \cos \theta_1 \cos \theta_2 - \frac{1}{2} \left[\frac{\sqrt{\mu + V_1}}{\sqrt{\mu + V_2}} + \frac{\sqrt{\mu + V_2}}{\sqrt{\mu + V_1}} \right] \sin \theta_1 \sin \theta_2, \quad (37)$$

while the corresponding Bloch waves $u(x)$ are of the form (5) with $p(x; \mu)$ being a T -periodic function in x .

Now we consider defect modes. Due to the symmetric nature of the defect, defect modes are either symmetric or antisymmetric. First we discuss symmetric defect modes. In the defect region $|x| < \frac{1}{2}D$, these modes have the form

$$u(x) = h \cos \sqrt{\mu + V_d} x, \quad (38)$$

where h is some constant. For this solution to decay as $|x| \rightarrow \infty$, the vector $[u(x), u'(x)]^T$ evaluated at $x = \frac{1}{2}D$ must be an eigenvector of the transfer matrix M with eigenvalue λ such that $|\lambda| < 1$. Thus,

$$M \begin{pmatrix} u \\ u' \end{pmatrix}_{x=D/2} = \lambda \begin{pmatrix} u \\ u' \end{pmatrix}_{x=D/2}. \quad (39)$$

The first equation of (39) gives λ as

$$\lambda = M_{11} - M_{12} \sqrt{\mu + V_d} \tan \theta_D, \quad (40)$$

where

$$\theta_D = \frac{1}{2} D \sqrt{\mu + V_d}. \quad (41)$$

On the other hand, recalling $\det(M) = 1$, the two eigenvalues of M thus are λ and $\frac{1}{\lambda}$. These two eigenvalues satisfy the trace relation

$$\lambda + \frac{1}{\lambda} = M_{11} + M_{22}. \quad (42)$$

When Equations (30)–(33) and (40) are substituted into the above relation, we then get the eigenvalue μ of symmetric defect modes through the following algebraic equation

$$\begin{aligned} (V_2 - V_1) \sqrt{\mu + V_d} \tan \theta_D &= \sqrt{\mu + V_1} \{ \mu + V_2 + (\mu + V_d) \tan^2 \theta_D \} \cot \theta_1 \\ &+ \sqrt{\mu + V_2} \{ \mu + V_1 + (\mu + V_d) \tan^2 \theta_D \} \cot \theta_2. \end{aligned} \quad (43)$$

Similarly, we can find the eigenvalue μ of antisymmetric defect modes through the equation

$$\begin{aligned} (V_1 - V_2) \sqrt{\mu + V_d} \cot \theta_D &= \sqrt{\mu + V_1} \{ \mu + V_2 + (\mu + V_d) \cot^2 \theta_D \} \cot \theta_1 \\ &+ \sqrt{\mu + V_2} \{ \mu + V_1 + (\mu + V_d) \cot^2 \theta_D \} \cot \theta_2. \end{aligned} \quad (44)$$

The above two equations give all defect modes in the piecewise-constant potential (25). The reader is reminded that when plotting μ from the above two equations, one should check that the corresponding λ from Equation (40) meets the condition $|\lambda| < 1$. Otherwise, the resulted solution $u(x)$ is unbounded as $|x| \rightarrow \infty$ and hence is not a defect mode.

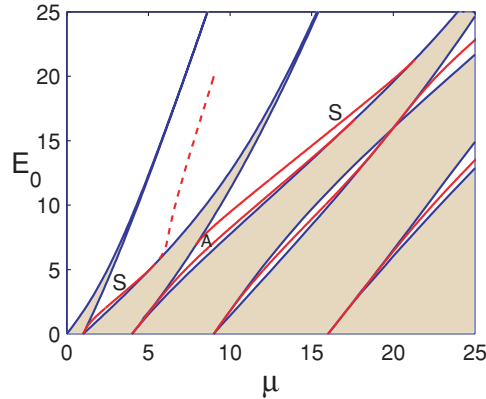


Figure 13. Defect-mode eigenvalues μ versus the applied dc field E_0 for the piece-wise-constant potential with a repulsive defect. Here the parameters are $T = \pi$, $D = \frac{1}{2}\pi$, $I_0 = 3$, and $I_D = 0$. The shaded region is the Bloch bands. The dashed line is a solution of Equation 43 but does not give localized defect modes. Letters “S” and “A” indicate branches of symmetric and antisymmetric defect modes, respectively.

As an example, we take specific parameter values $T = \pi$, $D = \frac{1}{2}\pi$, $I_0 = 3$, and $I_D = 0$, which give a potential resembling the one for a repulsive defect with $\epsilon = -1$ in Figure 8(a). For these parameters, the defect-mode eigenvalues as given by formulae (43), (44) and the condition $|\lambda| < 1$ are plotted in Figure 13 (solid lines). In the first bandgap, we found a branch of symmetric defect modes that exists when $0 < E_0 < 5.2$. In the second bandgap, there are two defect-mode branches. The lower one is antisymmetric and exists when $0 < E_0 < 16.7$, while the upper one is symmetric and exists when $6.9 < E_0 < 21.3$. These results are in perfect qualitative agreement with those in Figure 7 for the original potential (2). The third bandgap in Figure 13 is interesting in that as E_0 increases, this bandgap first opens up, then closes (at $E_0 \approx 16.7$), then opens up again. In this bandgap, Figure 13 shows a branch of antisymmetric defect modes. In the fourth bandgap, a branch of symmetric defect modes is found. In Figure 7 with the original potential, defect modes in the third and higher bandgaps were not examined.

One of the advantages of these analytical results is that they enable us to better understand the birth and death of defect-mode branches in repulsive defects. As an example, we reconsider Figure 13. In the first bandgap, a branch of symmetric defect modes merges into the edge of the Bloch band and disappears at $E_0 = 5.2$. This branch is a solution of Equation (43). Prior to merging, $|\lambda| < 1$ (as can be checked from Equation (40)). At the point of merging, $|\lambda| = 1$. Interestingly, we found that Equation (43) also admits other solutions above $E_0 = 5.2$. These solutions are also plotted in Figure 13 as a dashed curve. This dashed curve connects with the defect-mode branch (solid

curve) on the edge of the Bloch band at $E_0 = 5.2$, and it persists for all $E_0 > 5.2$ values. However, on this dashed curve, $|\lambda| > 1$. Thus, the dashed curve is not true defect modes. Rather, it corresponds to solutions $u(x)$ of Equation (26), which grow exponentially as $|x| \rightarrow \infty$. These results indicate that when a branch of defect modes disappears, it has to merge into the boundary of a Bloch band. After merging, localized defect modes become nonlocalized solutions and thus disappear.

7. Summary

In this paper, localized defect modes in one-dimensional optically induced photonic lattices are analyzed in detail. It is found that these defect modes bifurcate out from the edges of Bloch bands whenever a weak defect is present. If the defect is attractive, a defect mode bifurcates from the left edge of every Bloch band; while if the defect is repulsive, a defect mode bifurcates from the right edge of every Bloch band. When the defect is not weak, defect modes are studied by numerical methods. It is shown that in a repulsive defect, strongly localized defect modes arise when the lattice light intensity at the defect site is *nonzero* rather than zero. In addition, as the potential strength increases, defect modes disappear from lower bandgaps and appear in higher bandgaps. In an attractive defect, however, defect modes persist in every bandgap as the potential strength increases. Using a piecewise-constant potential model, defect modes are calculated analytically. The analytical results qualitatively explain the main features of numerical results. Experimental work on generation of lattices with defects and formation of defect modes as predicted above is currently underway.

Acknowledgments

The authors thank Dr. Shanhui Fan for stimulating discussions. This work was completed while J.Y. was visiting the Zhou-Pei-Yuan Center for Applied Mathematics in Tsinghua University. The hospitality of the Center is appreciated. This work was supported in part by the Air Force Office of Scientific Research, the National Science Foundation, and NASA EPSCoR grants.

References

1. J. D. JOANNOPOULOS, R. D. MEADE, and J. N. WINN, *Photonic Crystals: Molding the Flow of Light*, Princeton University Press, 1995.
2. P. RUSSELL, Photonic crystal fibers, *Science* 299:358 (2003).
3. D. N. CHRISTODOULIDES, F. LEDERER, and Y. SILBERBERG, Discretizing light behaviour in linear and nonlinear waveguide lattices, *Nature* 424:817–823 (2003).

4. D. K. CAMPBELL, S. FLACH, and Y. S. KIVSHAR, Localizing energy through nonlinearity and discreteness, *Phys. Today* 57:43–49 (2004).
5. A. B. ACEVES, C. DE ANGELIS, S. TRILLO, and S. WABNITZ, Storage and steering of self-trapped discrete solitons in nonlinear waveguide arrays, *Opt. Lett.* 19:332 (1994).
6. H. S. EISENBERG, Y. SILBERBERG, R. MORANDOTTI, A. R. BOYD, and J. S. AITCHISON, Discrete spatial optical solitons in waveguide arrays, *Phys. Rev. Lett.* 81:3383 (1998).
7. A. A. SUKHORUKOV and Y. S. KIVSHAR, Nonlinear localized waves in a periodic medium, *Phys. Rev. Lett.* 87:083901 (2001).
8. N. K. EFREMIDIS, S. SEARS, D. N. CHRISTODOULIDES, J. W. FLEISCHER, and M. SEGEV, Discrete solitons in photorefractive optically induced photonic lattices, *Phys. Rev. E* 66:046602 (2002).
9. J. W. FLEISCHER, M. SEGEV, N. K. EFREMIDIS, and D. N. CHRISTODOULIDES, Observation of two-dimensional discrete solitons in optically induced nonlinear photonic lattices, *Nature* 422:147 (2003).
10. D. MANDELIK, H. S. EISENBERG, Y. SILBERBERG, R. MORANDOTTI, and J. S. AITCHISON, Band-gap structure of waveguide arrays and excitation of Floquet-Bloch solitons, *Phys. Rev. Lett.* 90:053902 (2003).
11. D. NESHEV, E. OSTROVSKAYA, Y. KIVSHAR, and W. KROLIKOWSKI, Spatial solitons in optically induced gratings, *Opt. Lett.* 28:710 (2003).
12. H. MARTIN, E. D. EUGENIEVA, Z. CHEN, and D. N. CHRISTODOULIDES, Discrete solitons and soliton-induced dislocations in partially-coherent photonic lattices, *Phys. Rev. Lett.* 92:123902 (2004).
13. J. YANG, I. MAKASYUK, A. BEZRYADINA, and Z. CHEN, Dipole solitons in optically-induced two-dimensional photonic lattices, *Opt. Lett.* 29:1662 (2004).
14. R. IWANOW, R. SCHIEK, G. I. STEGEMAN, T. PERTSCH, F. LEDERER, Y. MIN, and W. SOHLER, Observation of discrete quadratic solitons, *Phys. Rev. Lett.* 93:113902 (2004).
15. Y. V. KARTASHOV, V. A. VYSLOUKH, and L. TORNER, Rotary solitons in Bessel optical lattices, *Phys. Rev. Lett.* 93:093904 (2004).
16. D. E. PELINOVSKY, A. A. SUKHORUKOV, and Y. S. KIVSHAR, Bifurcations and stability of gap solitons in periodic potentials, *Phys. Rev. E* 70:036618 (2004).
17. A. W. SNYDER, D. J. MITCHELL, L. POLADIAN, and F. LADOUCEUR, Self-induced optical fibers: Spatial solitary waves, *Opt. Lett.* 16:21 (1991).
18. S. F. MINGALEEV and Yu. S. KIVSHAR, Self-trapping and stable localized modes in nonlinear photonic crystals, *Phys. Rev. Lett.* 86:5474–5477 (2001).
19. U. PESCHEL, R. MORANDOTTI, J. S. AITCHISON, H. S. EISENBERG, and Y. SILBERBERG, Nonlinearly induced escape from a defect state in waveguide arrays, *Appl. Phys. Lett.* 75:1348 (1999).
20. R. MORANDOTTI, H. S. EISENBERG, D. DANDELIC, Y. SILBERBERG, D. MODOTTO, M. SOREL, C. R. STANLEY, and J. S. AITCHISON, Interactions of discrete solitons with structural defects, *Opt. Lett.* 28:834 (2003).
21. Z. CHEN and K. MCCARTHY, Spatial soliton pixels from partially incoherent light, *Opt. Lett.* 27:2019 (2002).
22. M. PETROVIC, D. TRÁGER, A. STRINIC, M. BELIC, J. SCHRÖDER, and C. DENZ, Solitonic lattices in photorefractive crystals, *Phys. Rev. E* 68:055601 (2003).
23. D. R. SMITH, R. DALICHAOUCH, N. KROLL, S. SCHULTZ, S. L. MCCALL, and P. M. PLATZMAN, Photonic band structure and defects in one and two dimensions, *J. Opt. Soc. Am. B* 10:314 (1993).

24. D. N. CHRISTODOULIDES and M. I. CARVALHO, Bright, dark, and gray spatial soliton states in photorefractive media, *J. Opt. Soc. Am. B* 12:1628 (1995).
25. M. SEGEV, M. SHIH, and G. C. VALLEY, Photorefractive screening solitons of high and low intensity, *J. Opt. Soc. Am. B* 13:706 (1996).
26. F. ODEH and J. B. KELLER, Partial differential equations with periodic coefficients and Bloch waves in crystals, *J. Math. Phys.* 5:1499 (1964).
27. Y. S. KIVSHAR, D. E. PELINOVSKY, T. CRETEGNY, and M. PEYRARD, Internal modes of solitary waves, *Phys. Rev. Lett.* 80:5032 (1998).

UNIVERSITY OF VERMONT,
TSINGHUA UNIVERSITY,
SAN FRANCISCO STATE UNIVERSITY

(Received April 11, 2005)

Queries

- Q1** Au: Please provide degree of the corresponding author.
- Q2** Author: Please check running head. Is it ok?
- Q3** Au: Please provide the place of publication in this reference.